Predator-prey plankton dynamics in turbulent flow past an obstacle

Alice Jaccod [1,*] Stefano Berti [2] Enrico Calzavarini [2] and Sergio Chibbaro [1]
[1]*Sorbonne Université, CNRS, Institut Jean Le Rond d'Alembert, F-75005 Paris, France*
[2]*Univ. Lille, ULR 7512, Unité de Mécanique de Lille Joseph Boussinesq (UML), F-59000 Lille, France*

Plankton constitutes the productive base of aquatic ecosystems and plays an essential role in the global carbon cycle. The impact of hydrodynamic conditions on the biological activity of plankton species can manifest in a variety of different ways, and the understanding of the basic effects due to multiscale complex flows still appears incomplete. Here we consider a predator-prey model of plankton dynamics in the presence of a turbulent flow past an idealized island, to investigate the conditions under which an algal bloom is observed and the resulting patchiness of plankton distributions. By means of direct numerical simulations, we explore the role of the turbulent intensity and of the obstacle shape. In particular, we focus on population variance spectra, and on their relation with the statistical features of the turbulent flow, as well as on the correlation between the spatial distribution of the planktonic species and velocity field persistent structures. We find that both the average biomass and local plankton dynamics critically depend on the relation between advective and biological timescales, confirming and extending previous results obtained in simpler flow settings. We further provide evidence that, in the present system, due to local flow action plankton accumulates in localized filamentary regions. Small turbulent scales are found to impact the statistics of plankton density fields at very fine scales, but the main global features of the population dynamics only weakly depend on the Reynolds number and are also found to be remarkably independent of the geometrical details of the obstacle.

I. INTRODUCTION

Planktonic populations are key to aquatic ecosystems, as they form the base of marine and lacustrine food webs [1], and play a central role in the climate, by taking part in the global carbon budget [2]. Plankton blooms, however, can also have major negative environmental and societal impacts, when involving harmful algae [3–5]. The modeling of plankton dynamics is therefore relevant to different studies, from both a fundamental and an applied point of view.

Among the physical-biological interactions controlling plankton blooms a prominent role is played by fluid transport. Understanding the role of laminar and turbulent flows on this phenomenon, both on the vertical [6–8] and on the horizontal [5,9–14] has attracted considerable interest. The complexity of the problem arises from the different processes acting on a very broad range of spatial and temporal scales [15–18]. Furthermore, the interplay between the fluid and biological dynamics is often subtle, making the prediction of the conditions for blooming nontrivial even in relatively simple theoretical models [5,8,19].

A distinctive feature characterizing plankton populations at the ocean surface is their patchiness, meaning their heterogeneous spatial distribution, due to lateral stirring and mixing, as revealed

---

*Corresponding author: alice.jaccod@upmc.fr

by satellite and ship-transect measurements of chlorophyll concentration (an indicator of the local phytoplankton biomass) [20–24]. Several efforts have been devoted to explain and numerically reproduce the statistical features, such as spectra, of plankton density fields. Using dimensional arguments, some theoretical predictions have been obtained, suggesting that the spectra of biological species in two-dimensional (2D) turbulent flows should be flatter than that of the velocity field, particularly for interacting species [20,25]. In numerical simulations, relying on an idealized model, the role of turbulent advection in the generation of patchiness was first put in evidence in [9], where some differences between phytoplankton and zooplankton were also observed, due to the typical biological timescale of the latter. The dominance of physical processes in structuring the spatial variability of plankton distributions was also reported in more realistic numerical studies (see, e.g., [23]). The picture emerging from previous experimental, theoretical, and numerical investigations, however, questions the universality of spectral slopes, pointing to large variability with respect to the physical and biological processes considered.

Turbulent flows of environmental interest, and particularly oceanic ones in the submesoscale and mesoscale ranges [horizontal size of $O(1–10)$ km and $O(10–100)$ km, respectively], are also characterized by the presence of coherent structures, in the form of eddies and filaments. Such structures have an important impact on biological dynamics, as they shape the spatial distribution of the different species [26]. Their effects on productivity depend on multiple factors. Based on kinematic-flow numerical simulations, and including nutrient dynamics, it has been argued that the confinement of plankton for sufficiently long time inside large eddies promotes biological growth [27,28]. Intense mesoscale stirring, on the other hand, can also reduce productivity in coastal upwelling systems, as shown using the same nutrient-phytoplankton-zooplankton (NPZ) model and flow fields from both satellite data and a regional model in the Benguela area [29]. This apparently counterintuitive result confirms previous remote-sensing observations [30,31] and is found to be due to relevant off-shore advection, through an analysis of the correlation between spatial features in plankton density fields and Lagrangian coherent structures.

Several important ideas to investigate the basic mechanisms underlying the effects of fluid motions on biological dynamics, as those mentioned above, were put forward in studies examining chemical and biological reactions in the presence of chaotic advection, in both closed and open flows [13,32–35]. In particular, these works highlighted the role of a special flow structure, the chaotic saddle, forming in open flows and capable of entraining fluid parcels for long time intervals [5,19,27,28,33,35]. Due to this property, when such flows are coupled to excitable biological dynamics [36,37], sustained blooms can take place [19]. As both fluid transport across the region of interest and biological growth are transient phenomena in that case, such a feature provides, in our opinion, an effective illustration of the nontrivial interplay between fluid and reactive dynamics. The above studies, however, considered kinematic velocity fields, namely, specified by a prescribed stream function. While such a simplified approach allows the description of some of the main flow features and offers reduced computational cost, it cannot account for complex flow dynamics, involving a whole range of temporal and spatial scales. Furthermore, it cannot be easily generalized to different geometries and boundary conditions.

In this work we explore the dynamics of a predator-prey model of plankton blooms displaying excitability, the so-called PZ (phytoplankton-zooplankton) model [36], in turbulent flows occurring in the wake of an obstacle. Our flow configuration shares some similarities with the one used to study plankton dynamics in the Canary region [5,27,28,38] using a kinematic flow (and NPZ model), but we take a more general perspective. In our setup, the obstacle mimics a generic island, rather than a specific one, and it could also equally represent another obstruction (e.g., a man-made construction) in a current. More importantly, our interest is mainly centered on the possible effects due to the spatiotemporal complexity of dynamical turbulent flows. In particular, we aim at identifying the minimal flow ingredients needed to sustain a bloom, and at characterizing how the latter could be affected by multiscale fluid properties. While investigating an idealized system, we avoid any bias possibly coming from the modeling of the small scales of the flow.

Furthermore, we have chosen the PZ model to leave apart possible effects linked to nutrient heterogeneities.

For this purpose we revisit some of the theoretical predictions and the numerical results obtained in simplified settings [13,19,35], to test their robustness against genuine multiscale flows. We then focus on the conditions for the occurrence of blooms and on their intensity in terms of global biomass produced, in progressively more turbulent 2D flows. By means of extensive fully resolved numerical simulations, we further investigate the statistical properties of plankton patchiness, quantifying variance spectra, and analyze the correlations between the spatial organization of prey (phytoplankton) and predator (zooplankton) populations with flow structures. Since it is not possible to perform resolved simulations of realistic configurations, we evaluate the impact of varying the size of the system. Finally, we consider the effect of changing the obstacle shape and assess the role of the roughness of its boundary, which had not been examined before to the best of our knowledge, in spite of its relevance in realistic situations.

This article is organized as follows. In Sec. II we introduce the mathematical framework of the problem, recalling the main dynamical features of the biological model adopted, and describing the link with the equations governing hydrodynamics. The numerical setup as well as the flow configuration and the main parameters used are illustrated in Sec. III. We present the results of our numerical study in Sec. IV, particularly discussing the impacts on the biological dynamics of the different turbulence regimes, of under-resolving the velocity field, and of the obstacle shape. Finally, discussions and conclusions are presented in Sec. V.

II. MATHEMATICAL FORMULATION

We investigate the growth dynamics of two planktonic species, the phytoplankton and the zooplankton, living in a fluid environment localized around islands, characterized by predator-prey interactions. Their spatiotemporal evolution can be conveniently described using coupled advection-reaction-diffusion equations.

As for the reaction kinetics, a simple model accounting in an effective way for bloom dynamics was proposed in [36] based on the properties of excitable media [39,40]. This model, also known as the PZ (for phytoplankton-zooplankton) model, provided useful to reproduce the main dynamical features of red tides. Its two basic ingredients are the trigger mechanism, represented by the interaction between the phytoplankton growth rate and the grazing rate of zooplankton, which gives rise to the prey population outbreak, and the refractory mechanism, represented by the growth of zooplankton, which causes the system return to the initial equilibrium state.

In well-mixed conditions, calling $P = P(t)$ and $Z = Z(t)$ the population densities of phytoplankton and zooplankton, respectively, the evolution equations read

$$\frac{dP}{dt} = rP\Big(1 - \frac{P}{K}\Big) - R_m Z \frac{P^2}{P^2 + \kappa^2}, \tag{1a}$$

$$\frac{dZ}{dt} = \gamma R_m Z \frac{P^2}{P^2 + \kappa^2} - \mu Z. \tag{1b}$$

The term $rP(1 - P/K)$ represents the gross rate of production of phytoplankton, called primary production PP, and is expressed by a logistic growth function, with a maximum specific growth rate r and a carrying capacity K. Predation of phytoplankton is represented by a Holling Type III function [41], where R_m is the maximum specific predation rate and κ determines how quickly that maximum is attained as the prey population density increases. The rate of zooplankton production is controlled by the population density of phytoplankton, with γ representing the ratio of biomass consumed to biomass of new herbivores produced. The rate of zooplankton removal, by natural death and predation from higher organisms, is called μ. To display excitability, the PZ model must have at least two different timescales: to initiate an outbreak, the phytoplankton growth rate must be larger than the predation rate by the zooplankton population.

To consider the previous reactive dynamics in a fluid flow, it is necessary to specify the evolution equation for the velocity field and the influence of the latter on the population densities, $P(\boldsymbol{x}, t)$ and $Z(\boldsymbol{x}, t)$. It is useful to formulate the complete model in nondimensional variables. For this purpose, we introduce a characteristic length l_0 and a typical velocity u_0, from which the typical time is $t_0 = l_0/u_0$. We then consider an incompressible 2D flow defined on a square domain of side L, in the presence of a circular obstacle (of radius l_0) representing an island, which is the solution of the Navier-Stokes equation with the appropriate boundary conditions (see Sec. III). The nondimensional form of the latter equation and of the incompressibility condition is

$$\partial_t \boldsymbol{u} + (\boldsymbol{u} \cdot \boldsymbol{\nabla})\boldsymbol{u} = -\boldsymbol{\nabla} p + \frac{1}{\text{Re}} \boldsymbol{\nabla}^2 \boldsymbol{u}, \tag{2a}$$

$$\boldsymbol{\nabla} \cdot \boldsymbol{u} = 0, \tag{2b}$$

where $\boldsymbol{u}(\boldsymbol{x}, t)$ is the dimensionless fluid velocity field, p is pressure, and $\text{Re} = u_0 d/\nu$ the Reynolds number based on the obstacle diameter $d = 2l_0$, with ν the viscosity coefficient.

As we have neglected any feedback effects of the planktonic species on the velocity field in Eq. (2a), as it is reasonable considering their weakness in realistic conditions, the link between the biological and fluid dynamics, is realized only by advection. This implies that the time derivatives in Eqs. (1a) and (1b) now need to be interpreted as material derivatives. Note that in the following we will also add a diffusivity term to both equations, with a diffusion coefficient D (equal for the two species), possibly due to swimming behavior. Proceeding as before and further normalizing the population densities with the carrying capacity K, we obtain

$$\partial_t P + \boldsymbol{u} \cdot \boldsymbol{\nabla} P - \frac{1}{\text{ReSc}} \boldsymbol{\nabla}^2 P = \epsilon \left(\beta P(1 - P) - \delta Z \frac{P^2}{P^2 + \chi^2} \right), \tag{3a}$$

$$\partial_t Z + \boldsymbol{u} \cdot \boldsymbol{\nabla} Z - \frac{1}{\text{ReSc}} \boldsymbol{\nabla}^2 Z = \epsilon \gamma Z \left(\delta \frac{P^2}{P^2 + \chi^2} - \lambda \right), \tag{3b}$$

where $\text{Sc} = \nu/D$ is the Schmidt number, $\beta = rl_0/u_0$, $\delta = R_m l_0/u_0$, $\chi = \kappa/K$, $\lambda = \mu l_0/(u_0\gamma)$. In addition, we have introduced the parameter ϵ in front of the reaction terms, which allows us to perform a parametric study in a simple way, by artificially changing the ratio between the advective timescale and the biological activity one. In the following we will always work with dimensionless variables and we will set ϵ to 1, unless explicitly stated.

The dynamics resulting from Eqs. (2a) and (2b) and (3a) and (3b) are generally highly nontrivial, which severely limits the possibility to perform analytical calculations. Some results concerning the transport and mixing of planktonic species, nevertheless, have been previously obtained in simpler configurations, using the tools of dynamical systems theory, and will serve us as a guide for our analysis [13,34,42,43]. While the analytical resolution of the full dynamics is not possible, it is instructive to recall some important results concerning the reactive dynamics in the absence of flow [36]. From Eqs. (1a) and (1b), one can obtain the fixed points of the PZ model: $(P_1, Z_1) = (0, 0)$, $(P_2, Z_2) = (1, 0)$ and $(P_3, Z_3) = (P_{eq}, Z_{eq})$ where $P_{eq} = \chi\sqrt{\lambda/(\delta - \lambda)}$ and $Z_{eq} = \beta(1 - P_{eq})(P_{eq}^2 + \chi^2)/(P_{eq}\delta)$, expressed in nondimensional variables. The first one represents the extinction of both species, (P_2, Z_2) gives the equilibrium value of P in the absence of Z, and (P_3, Z_3) is the stable pre-outbreak state of species coexistence. From stability analysis, it emerges that (P_1, Z_1) and (P_2, Z_2) are saddle points, while (P_3, Z_3) is a stable equilibrium point when appropriate parameter values are used (see [36] and Sec. III).

III. NUMERICAL SETUP

The flow field is assumed to be initially uniform and unidirectional, $\boldsymbol{u} = u_0\hat{\boldsymbol{x}}$. In the following we will also refer to the streamwise (x) and the cross-stream (y) directions as the longitudinal and the transversal ones, respectively. The reference dimensional and nondimensional values we adopted for the biological model [19] are reported in Table I.

TABLE I. Parameters used in the biological model. The symbols adopted for the nondimensional quantities appear in parentheses in the first column. The values are consistent with typical oceanic ones.

Parameter	Value	Dimensionless value
K	$108 \, \mu\mathrm{g} \, \mathrm{Nl}^{-1}$	1
$r \, (\beta)$	$0.3 \, \mathrm{day}^{-1}$	4.285
$R_m \, (\delta)$	$0.7 \, \mathrm{day}^{-1}$	10
$\alpha \, (\chi)$	$5.7 \, \mu\mathrm{g} \, \mathrm{Nl}^{-1}$	0.053
$\mu \, (\lambda)$	$0.0024 \, \mathrm{day}^{-1}$	3.428
γ	0.01	0.01

Once the biological parameters fixed, the control parameters are the Reynolds and Schmidt numbers. Using for both of them the realistic values for oceanic conditions is beyond the capabilities of current direct numerical simulations (DNS), so that moderate Re numbers have to be chosen. Yet we have investigated different Reynolds-number flows to analyze the possible impact of this choice. Based on the effective diffusivity of swimming algae [44–46], we appraise the Sc number in the range $\approx(10^2$–$10^3)$. Here, due to numerical constraints, we fix $\mathrm{Sc} = 10^2$. From this parameter, the smallest relevant scale, i.e., the Batchelor scale, is $\ell_B = \ell_\nu \mathrm{Sc}^{-1/2}$, where ℓ_ν is the viscous dissipation cutoff. Assuming that the turbulent dynamics are governed by a direct enstrophy cascade (see also Sec. IV D), the latter can be estimated as $\ell_\nu = (\nu^3/\langle \eta_\nu \rangle)^{1/6}$, where $\langle \eta_\nu \rangle$ is the mean enstrophy flux [47].

All the dynamical equations, Eqs. (2a) and (2b) and (3a) and (3b), are solved through the open-source code Basilisk [48]. The adopted boundary conditions are such that inflow and outflow conditions are imposed on the left and right side of the domain, while free-slip conditions hold at the boundaries in the y-direction. On the obstacle we have a no-slip condition for the velocity, while a no-flux condition is imposed for the two scalars, which are furthermore kept at the equilibrium values (P_{eq}, Z_{eq}) at all sides of the domain. Further details on the numerical approach and boundary conditions are provided in Appendix A. For the initial conditions, we fix the longitudinal advecting velocity to the uniform inflow value u_0, while the transversal one is zero. Following [19], the scalar fields are initially set to their equilibrium values. At a later time $t^* > 0$, once the flow is in statistically stationary conditions, to mimic the arrival of a small phytoplankton population, we let a localized patch of P density enter the system from the left of the obstacle. Its spatial distribution is chosen to be of the form

$$P(\mathbf{x}, t^*) = P_{eq} + P_a e^{(-((x-x_0)^2 + (y-y_0)^2)/w^2)}, \tag{4}$$

where $P_a = 0.5$ is the amplitude of the excitation, $(x_0, y_0) = (-2, 0.5)$ its location, and $w = 0.9$ ($\simeq l_0$) its width. From a numerical point of view, such a direct perturbation of the P field is the simplest option to model an outbreak, and for this reason it is commonly adopted [19,36]. Although it may argued that it could correspond to the activation of some dormant phytoplankton individuals, as already recognized in [36], its degree of realism is limited. Interestingly, however, while possibly more realistic choices of the triggering mechanism can give rise to qualitatively different dynamics, the excitable nature of the system is unaffected by their specific forms [36]. In Sec. IV C the possible effect of changing the location and the amplitude of the P initial patch is discussed.

In Fig. 1 we show some visualizations of the vorticity and phytoplankton fields for the simulation at the highest Reynolds number considered. The planktonic patch is introduced at $t^* = 110$, and it takes a certain time to overtake the obstacle and cover the domain with complex filamentary structures, as has been pointed out in [34]. The plankton patchiness follows the spatial organization of the flow: the correlation between the phytoplankton density and coherent structures is apparent in
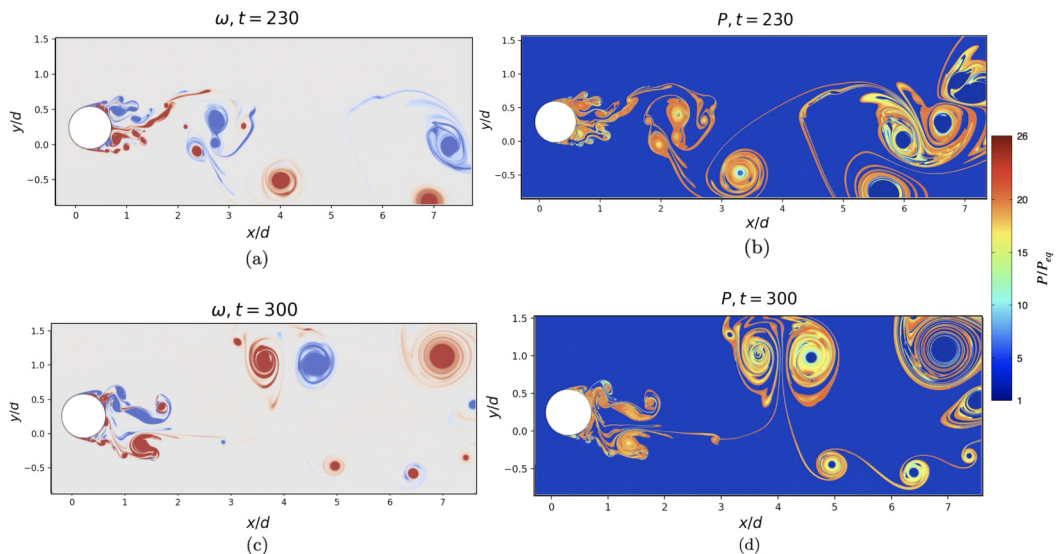
FIG. 1. Vorticity field ω (a), (c) and phytoplankton density P (b), (d) at $t = 230$ (top panels) and $t = 300$ (bottom panels) at Re = 20 000. In the left column blue stands for clockwise circulation and red for counterclockwise. The color bar refers to the panels in the right column.

the figure, and it will be quantitatively investigated in the following. It is here important to stress the transient character of the fluid motion: the flow structures, after spending some time in the vicinity of the obstacle, continuously leave the domain through the right side.

IV. RESULTS

A. Flow regimes

The flow past a cylindrical obstacle is a classical flow configuration in fluid mechanics. In its 2D version, it has already been considered as a relevant model to describe the wake behind an island to investigate the population dynamics of micro-organisms at the surface of the ocean, although through a prescribed stream function [5,27,28,49]. Let us recall that the flow becomes unsteady at moderate Reynolds numbers, and for $40 < \text{Re} < 1000$ vortices are periodically shed from the obstacle, while for Re > 1000, the separated flow becomes increasingly more turbulent displaying spatially and temporally irregular behavior [50]. In the periodic regime, a relevant nondimensional parameter is the Strouhal number, $\text{St} = nd/U$, in which U is the free-stream velocity intensity and n the vortex-shedding frequency. The typical flow timescale is thus $T = 1/n$, which gives the time interval between the appearance of two vortices of the same sign. In the absence of the biological scalar fields, at Re = 400, we obtained a periodic flow, as the one used in kinematic simulations [5,27,28,49], with $T \simeq 8$ in nondimensional units, or St $\simeq 0.23$, in good agreement with experiments in a homogeneous nonrotating tank (where St ≈ 0.21 [51]). Increasing the Re number, the flow becomes less and less regular, and eventually the periodic behavior is lost. In the present work, we have considered three simulations with the following Reynolds numbers: (1) Re = 400 ($N = 2^{11}$), (2) Re = 2000 ($N = 2^{12}$), and (3) Re = 20 000 ($N = 2^{14}$), where we indicate in parentheses the maximum grid resolution N for each case.

B. PZ model

The excitable character of the biological model can be appreciated by considering the temporal evolution of the system in the presence of the obstacle but in the absence of flow [$\boldsymbol{u} = 0$ in Eqs. (3a) and (3b)] with the described initial condition for the patch [see Fig. 2(a)]. As in [19,36], here the
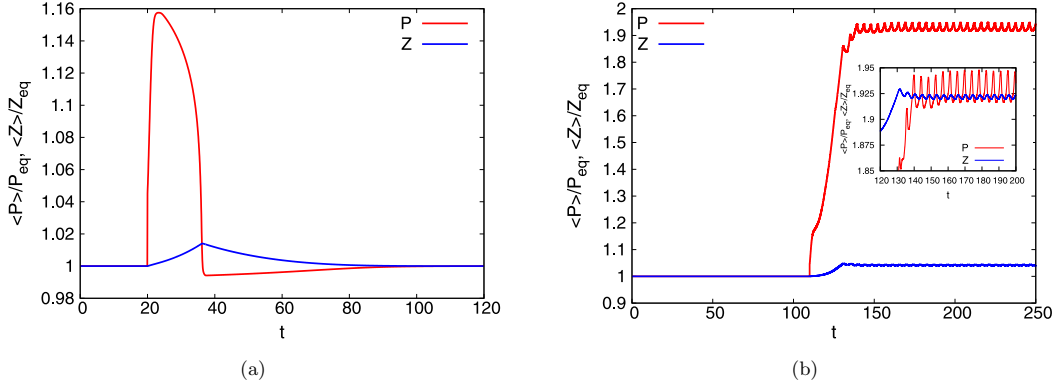
FIG. 2. Population densities of phytoplankton P and zooplankton Z, averaged in space and normalized by the corresponding equilibrium values, in the absence (a) and in the presence (b) of flow (at Re = 400). In the right panel the perturbation is introduced at $t^* = 110$. In the corresponding inset the Z curve is shifted above, to superpose it to the P curve, to highlight the delay of the zooplankton growth with respect to the phytoplankton one also in the presence of a flow.

outbreak is caused by a direct perturbation of P via a sudden increase of its density. The response of the planktonic species, initially at their equilibrium density values P_{eq} and Z_{eq} everywhere in the domain, is characterized by a fast initial growth of the spatially averaged phytoplankton density, followed by a slower return to the equilibrium, caused by the (slower) growth of zooplankton. This picture is possible because the two species evolve on different timescales, given the presence of parameter γ in Eq. (1b) [or, analogously, in Eq. (3b)], which limits the zooplankton predation efficiency and thus allows phytoplankton to escape the Z control to reach the carrying capacity. Therefore, we see that due to excitability plankton growth is a transient phenomenon in this system.

C. Coupled biological and fluid dynamics

Stirring and advection by the fluid flow have remarkable consequences on the biological dynamics. As shown in Fig. 2(b) at Re = 400, the combined (transient) effects of fluid transport and population growth give rise to a permanent excitation of the predator-prey system. Both P and Z now reach spatially averaged densities that are considerably larger than their equilibrium values. The temporal behavior is dictated by the vortex shedding, with period $T \simeq 8$ (in nondimensional units), to which the biological dynamics is slaved. Indeed, as shown in Fig. 2(b), both populations oscillate regularly in time with period T. This result confirms the outcomes of previous works [13,19,34], where the same change of behavior was investigated using kinematic flows (in slightly different configurations) and a basic mechanism was proposed in terms of the existence of a chaotic saddle, namely, a flow structure generated by the presence of the obstacle, in which fluid parcels remain trapped for very long time.

We briefly recall here the main elements at the origin of the phenomenon (see [35] for a more complete description). The chaotic saddle, being associated with the presence of straining points where velocity gradients compete with reaction-diffusion spreading, can determine the confinement of the fast-growing species into stable filaments. This localization of the prey distribution, with respect to that of the slower-growing predator, favors persistence. The open nature of the system then prevents filaments from becoming space-filling, which is needed to maintain the excitation. In a closed domain, in fact, the stretching and folding of filaments operated by the flow would homogenize the population distributions, bringing them close to the no-flow situation after some time, and hence cause the end of the excitation. The basic phenomenology has been already investigated for plankton dynamics in kinematic flows [43].
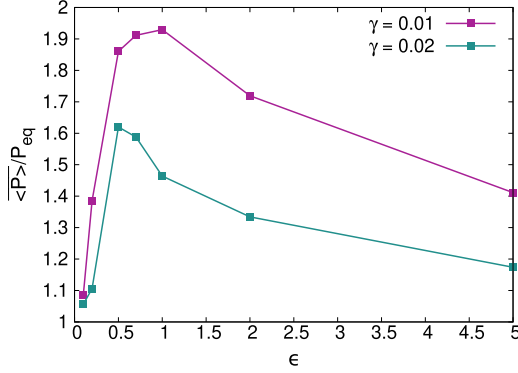
FIG. 3. Phytoplankton population, averaged in space and time, as a function of the ratio between the transport and the biological activity timescales ϵ, for two values of the predation efficiency γ at Re = 400.

As suggested by dynamic visualizations (see the Supplemental Material [52]), however, the plankton growth here appears to start on the side of the obstacle facing the incoming flow, rather than just in the chaotic saddle after it. Indeed, the phytoplankton perturbation is introduced in front of the obstacle and first encounters the straining point upstream of it, close to which it gets trapped. This might produce quantitative differences in the blooming dynamics, or indicate a dependence on initial conditions. To address this issue, several tests have been performed to study the impact of the specific form of the P initial condition. The system response turned out to be independent of the amplitude P_a of the initial perturbation (no appreciable differences arise by varying this parameter in the range $0.1 \leqslant P_a \leqslant 0.5$), as well as on its size w. Regarding its location, i.e., (x_0, y_0), the algal bloom occurrence and its permanent character have been found for different values of x_0: initializing the perturbation in front of the obstacle or behind it does not affect the dynamics of the scalar fields, provided that $|x_0| < 2.5d$. For initial positions further downstream of the obstacle, the patch is advected away by the flow without giving rise to a permanent excitation. Our results show therefore that the characteristics of the bloom are largely independent of the precise mechanism trapping plankton, provided the hydrodynamic timescale is much larger than the biological one. This result motivated us to study also various laminar cases at $2 \lesssim \text{Re} \lesssim 10$ (results not shown for the sake of brevity), since these flows are not chaotic but they have two stagnation points in front of and behind the obstacle. While the results are globally different from the turbulent ones, as there is no mixing, interestingly, the plankton still displays the same quantitative growth as in the chaotic case.

Then we have investigated through several simulations the impact of the biological properties, namely, the ratio of the transport to the biological activity timescales ϵ, and the ratio of biomass consumed to biomass of new herbivores produced, i.e., the predation efficiency γ. The results are reported in Fig. 3. The dependence of the spatially and temporally averaged P on γ is evident: no matter the value of ϵ, the mean global value of phytoplankton $\overline{\langle P \rangle}$ is higher for $\gamma = 0.01$ than for $\gamma = 0.02$, i.e., for a smaller predation efficiency. We checked that such a feature is general, considering different increasing values of γ. Beyond a limiting value $\gamma = 0.05$, the grazing by the zooplankton dominates and the system dynamics cannot sustain a permanent excitation. The phytoplankton bloom is in that case only a transient event, as in the absence of flow. The impact of ϵ is more complex, as also suggested by [19]. Independently of γ, an optimal value $\epsilon^* = O(1)$ of this ratio exists. It is attained when the transport by the flow is slower than phytoplankton growth (as $\beta > 1$, i.e., $t_0 > r^{-1}$, and $\epsilon \simeq 1$). For values of ϵ much smaller or much larger than ϵ^*, we observe a tendency to recover the equilibrium state, which can be understood as follows. Decreasing ϵ corresponds to making advection faster (or growth slower). In this case, the initial phytoplankton patch is deformed by stirring and diffusion but soon decays downstream of the obstacle, as the
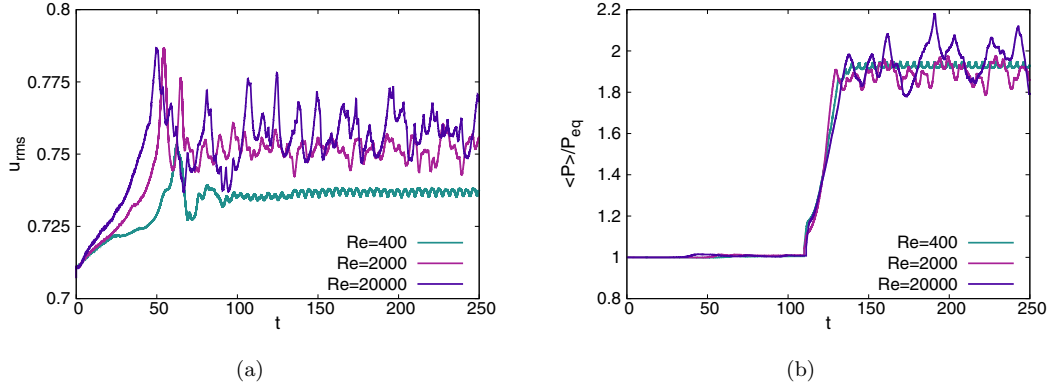
FIG. 4. (a) Root-mean-square fluid velocity u_{rms} and (b) spatially averaged phytoplankton density $\langle P \rangle$, normalized by the equilibrium value P_{eq}, vs time for increasing Re numbers. In the right panel, the phytoplankton patch is introduced at $t^* = 110$.

biological dynamics are too slow to sustain its growth. In the opposite limit of large ϵ, corresponding to very slow flow (or very fast growth), a sudden excitation occurs upstream of the obstacle but the two populations start to get back to their equilibrium states before reaching the obstacle and so when they are entrained in the wake the initial abundance of phytoplankton has been already partially consumed, resulting in a smaller value of the average biomass in the system. The behavior for $\epsilon \ll \epsilon^*$ is consistent with the transition to permanent excitation previously detected using a kinematic perturbed jet [19]. The behavior at $\epsilon \gg \epsilon^*$, instead, points to a second transition, to de-excitation, which could not be found in [19], likely due to the specific topology of the flow employed, but which was documented for a different excitable medium in the presence of a blinking vortex-sink flow [35].

D. Role of turbulence and impact of Re

In a realistic geophysical configuration, the Reynolds number is typically huge ($10^8 \lesssim \mathrm{Re} \lesssim 10^{10}$). While it is not possible to carry out fully resolved simulations of flows at such large values of Re, it is crucial to understand if the basic features detected at moderate Re are robust with respect to the increase of this control parameter. We investigated the role of the turbulent dynamics using the fixed values $\epsilon = 1$ and $\gamma = 0.01$ of the coupling parameters discussed in Sec. IV C. As can be seen in Fig. 4(a), when Re $\geqslant 2000$ the root-mean-square (rms) flow intensity u_{rms} loses its periodicity and displays a highly irregular temporal behavior. At Re $= 20\,000$ the vortices do not travel along a straight path but are now deflected in the transversal direction, above and below the center line (see Fig. 1). Due to the spatial and temporal complexity of the flow, the planktonic populations no longer oscillate periodically in time, and the filamentary structures appear thinner and more convoluted, especially close to the obstacle. This feature is reflected in the measure of the globally averaged population density, $\langle P \rangle$ [Fig. 4(b)], for which the amplitude and irregularity of fluctuations are modified by the increased chaoticity of the flow, in spite of a weak dependence of its (temporal) mean value on Re.

In the following, we present the results of a deeper analysis about the local properties of plankton fields. In particular, we aim at investigating their correlation with the underlying flow. We focus on simulation 3 (at Re $= 20\,000$), representative of the fully turbulent regime, but we will also perform some comparisons with the results in the periodic regime of simulation 1 (at Re $= 400$).

We first consider the spectra of scalar variance and kinetic energy. Figure 5(a) reports one-dimensional spectra of velocity (u_x, u_y) and scalar (P, Z) fluctuations, in the transverse direction (with respect to the mean flow), computed in the subdomain $1.5d \leqslant x \leqslant 10d$ (with d the obstacle
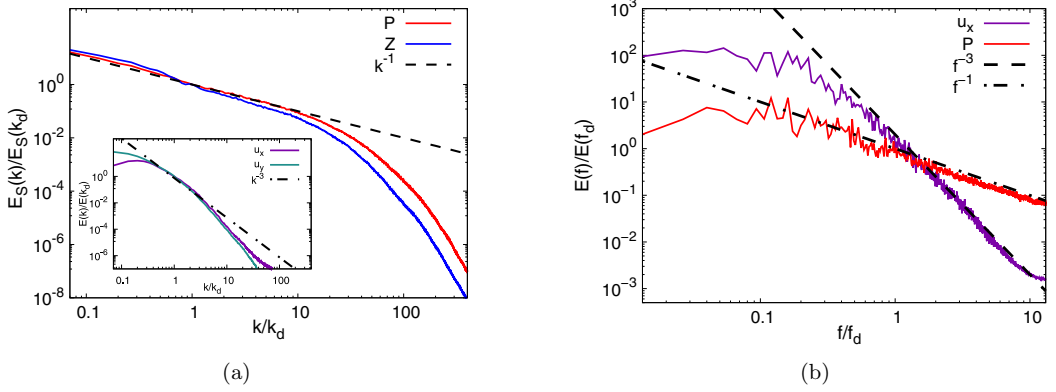
FIG. 5. (a) Spatial spectra of phytoplankton and zooplankton fluctuations $E_S(k)$ (with $S = P, Z$), and spectra of velocity component fluctuations $E(k)$ (inset) at Re $= 20\,000$. All these spectra are normalized by the value corresponding to k_d, the wave number associated with the obstacle diameter d. The spectra are computed along the y-direction and then averaged for $1.5d \leqslant x \leqslant 10d$ and $150 \leqslant t \leqslant 300$. (b) Power spectra in the frequency domain $E(f)$ of longitudinal velocity u_x and phytoplankton fluctuations at Re $= 20\,000$, normalized by the value corresponding to f_d. Note that $f_d = n/St$, where n is the vortex-shedding frequency.

diameter). Note that the Fourier transform is performed along the y direction at several fixed longitudinal positions x and that the resulting spectra are subsequently averaged in the x direction. To improve the statistics, we further perform a temporal average of the latter, in the time interval $150 \leqslant t \leqslant 300$ (in nondimensional units), in which the system is in a statistically stationary state. Energy spectra are compatible with a scaling $E(k) \sim k^{-3}$ over approximately one decade, pointing to the existence of a smooth flow and a direct enstrophy cascade [53], with an injection scale k_d corresponding to the diameter of the obstacle. At the highest wave numbers they tend to be steeper, when dissipation starts dominating. We remark that, for our discussions about the interplay between fluid and biological dynamics, the precise slope of $E(k)$ is not expected to play a major role, as long as the spectrum is steep enough. In fact, both for a spectrum scaling as k^{-3} and for a steeper one, the flow possesses a single timescale, determined by the strain (which essentially acts at the largest scales, in both these cases).

The wave number spectra of plankton populations, and particularly that of phytoplankton, are commonly used to characterize biological patchiness. Several experimental measurements, obtained using transects from research vessels and satellite images of the sea color (a proxy for phytoplankton concentration), have been performed in different regions [20–24]. While they all provide evidence of a power-law behavior $\sim k^{-n}$, different values of the exponent are reported, ranging from $n = 1$ to $n = 3$, which suggests that different physical and biological processes may be relevant for plankton spatial variability, in different conditions. In our simulations, for both planktonic species we find a spectrum close to $E_S(k) \sim k^{-1}$ in a wide range extending for approximately two decades, starting from the largest scale. At the smallest scales, dissipative effects appear to dominate. We have therefore found that the distribution across scales of the variance of passive reactive scalars is the same as that of passive nonreactive ones [54] (more details are given in Appendix B). The observed behavior is in agreement with theoretical predictions for two interacting species evolving in a 2D smooth turbulent flow [25]. This result implies that population dynamics somehow reduce patchiness at large scales, giving rise to "whiter" spectra of the scalar fluctuations, meaning flatter than for the turbulent flow. In Fig. 5(b) we also show the power spectra in the frequency domain for phytoplankton and the longitudinal velocity component, which confirm the above scaling behavior even more accurately. The Fourier transform is here performed in the time domain by collecting the data at a distance $x = 5d$ downstream of the obstacle and then averaging the resulting spectra in the y direction.
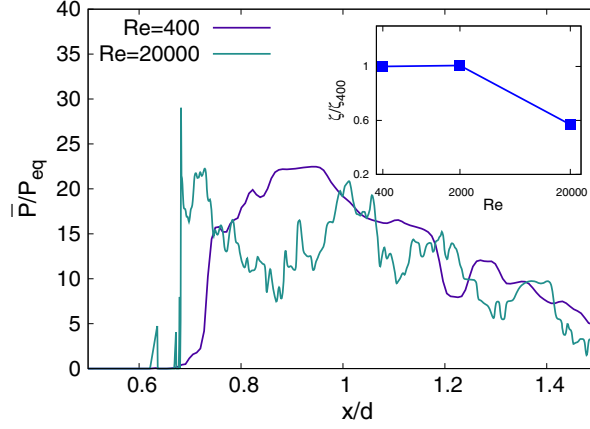
FIG. 6. Transects of time-averaged (in the range $150 \leqslant t \leqslant 300$) phytoplankton density, normalized by the equilibrium value, $\overline{P}/P_{eq}$, at the center line $y/d = 0$ for Re $= 400$ and Re $= 20\,000$. Inset: ratio $\zeta = \beta_{\text{eff}}/\langle\eta_v\rangle^{1/3}$ (see text), normalized by its value at Re $= 400$ for the three simulations (Re $= 400, 2000, 20\,000$).

Having quantified the scale-by-scale energetic content of the planktonic populations, we now turn to their spatial features. Indeed, the characteristic spatial patterns of the P and Z fields are a consequence of the timescales over which they respond to changes in their environment caused by the turbulent flow [9]. While global quantities of the planktonic species share a similar qualitative behavior in all our simulations (see Fig. 4), the amplitude and frequency of the fluctuations grow with Re. To inspect the effect on spatial features of increasing the Reynolds number, we can consider a horizontal cut along the line $y/d = 0$ to obtain a transect of the phytoplankton density in the vicinity of the obstacle. As is evident from Fig. 6, while for Re $= 400$ the population density field appears quite smooth, for Re $= 20\,000$ it appears considerably more jagged, displaying much stronger gradients. Some insight into this change of behavior can be gained by adapting a criterion, originally developed in the framework of linear-decay chemical reactions (with rate b) in laminar flows, to identify the so-called smooth-filamental transition [33]. In a nutshell, the theory, constructed in a Lagrangian reference frame, is based on the comparison between the largest Lyapunov exponent of the flow λ and the chemical (biological) Lyapunov exponent ($b = \lambda_c$), quantifying the exponential growth rate of the chemical concentration (biological population density), which allows to obtain the Hölder exponent ζ of the reactive field as

$$\zeta = \min\left\{\frac{b}{\lambda}, 1\right\}. \tag{5}$$

If $\zeta = 1$ the field is smooth (differentiable), while for $0 < \zeta < 1$ it is filamental.

In the context of the present study, a simple possibility to estimate the corresponding quantities is by dimensional arguments. The Lyapunov exponent of the flow should be proportional to the inverse of the fastest fluid timescale [55]. Consistent with the occurrence of a direct enstrophy cascade (see Fig. 5), we then take $\lambda \sim \langle\eta_v\rangle^{1/3}$ (with η_v the enstrophy flux). For the biological dynamics we consider an effective phytoplankton growth rate $\beta_{\text{eff}} = \partial_t\langle P\rangle/\langle P\rangle$, computed in the early growth regime ($110 \leqslant t \leqslant 130$ in nondimensional units) before the statistically steady state. In the inset of Fig. 6 our estimation of ζ, normalized by the value at the smallest Reynolds number ζ_{400}, is plotted versus Re for simulations 1, 2, and 3. In spite of the limitations of our dimensional approach, the criterion turns out to be effective in capturing the transition. A clear decrease is found between the first two values of Re, for which the ratio is close to unity, and the largest one, for which it is definitely smaller. We then conclude that the filamentary distribution of phytoplankton is a direct consequence of the increasing turbulent character of the flow.
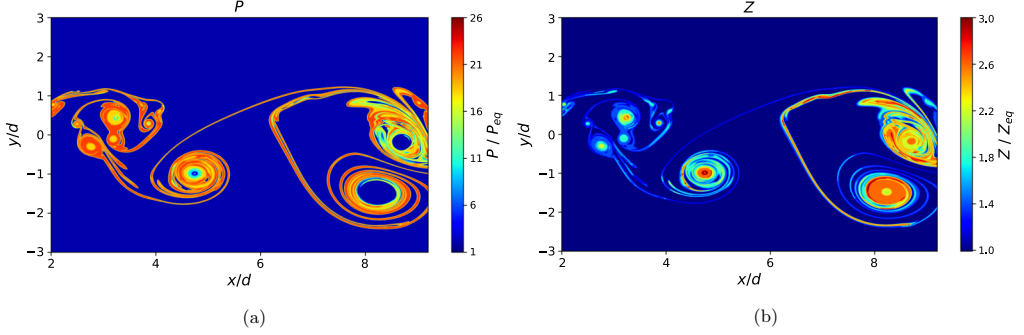
FIG. 7. Instantaneous phytoplankton P (a) zooplankton Z (b) density fields, for Re $= 20\,000$ at $t = 230$, in the statistically steady state.

Based on the previous observations about the relationship between the statistical features of the turbulent and biological dynamics, it is now interesting to explore how the flow and scalar fields are correlated in space, in terms of structures. For this purpose, at a given time in the statistically stationary state, we analyze both the phytoplankton and zooplankton spatial distribution at Re $= 20\,000$ in Fig. 7. As has been already observed in Fig. 1, both P and Z fields display structures similar to those present in the vorticity field. Very close to the obstacle, several vortices of different sizes are present, somehow connected by filaments. Further downstream of the obstacle, such vortices grow and interact among each other, giving rise to two large and more separated eddies. Phytoplankton winds around vortices, mainly concentrating in filaments, immediately downstream of the obstacle, and it progressively leaves the vortex cores, in which P is at the equilibrium value P_{eq} [Fig. 7(a)]. The zooplankton distribution parallels that of P, in terms of correlation between its extremal values and flow structures [Fig. 7(b)]. However, maxima of Z correspond to minima of P, such as in eddy cores. The resulting picture is therefore due to two combining effects. The flow structures entrain the two scalars and transport them across the domain. The predator-prey biological interactions determine, locally, the relative abundance of the two species: where zooplankton grows, it consumes phytoplankton; where Z is absent, instead, P can grow more.

Similar results were previously found coupling the NPZ model (including nutrient dynamics) with a kinematic flow model [28], essentially in the same geometrical configuration. Still for inflow densities at the equilibrium values, it was reported that phytoplankton tends to be localized mostly in the periphery of vortices, as in our study, which seems indicative of the generality of fluid transport and stirring mechanisms leading to filament formation.

A more quantitative analysis of the correlation between the flow and the phytoplankton distribution was performed by considering an Eulerian quantity, the turbulent kinetic energy ($\mathcal{K}_E$), which is strictly linked to the flow stirring, since it is expected that more energetic turbulent areas would also present stronger horizontal stirring [30,31]. Denoting $u_i'(\boldsymbol{x}, t) = u_i(\boldsymbol{x}, t) - \bar{u}_i(\boldsymbol{x})$ (with $i = x, y$) the components of the fluctuating velocity field and with the overbar the temporal average over the time interval $t \in [150, 300]$, the $\mathcal{K}_E$ field is given by

$$\mathcal{K}_E(\boldsymbol{x}, t) = \tfrac{1}{2}[u_x'(\boldsymbol{x}, t)^2 + u_y'(\boldsymbol{x}, t)^2]. \tag{6}$$

Similarly to what is done in [56], we compute the average and the probability distribution function (PDF) of $\tilde{P} = P/P_{eq}$ conditioned on $\mathcal{K}_E$, over the time interval $t \in [150, 300]$. As shown in Fig. 8, we find that the phytoplankton distribution and the turbulent kinetic energy are positively correlated: the PDF conditioned on $\mathcal{K}_E$ exhibits a peak, for a value of P essentially independent of $\mathcal{K}_E$, whose height increases with $\mathcal{K}_E$. The conditioned average shows a growth trend as a function of $\mathcal{K}_E$, which means that phytoplankton tends to concentrate in regions associated with high values of $\mathcal{K}_E$, i.e., characterized by intense flow stirring. The above evidence then suggests that the stirring
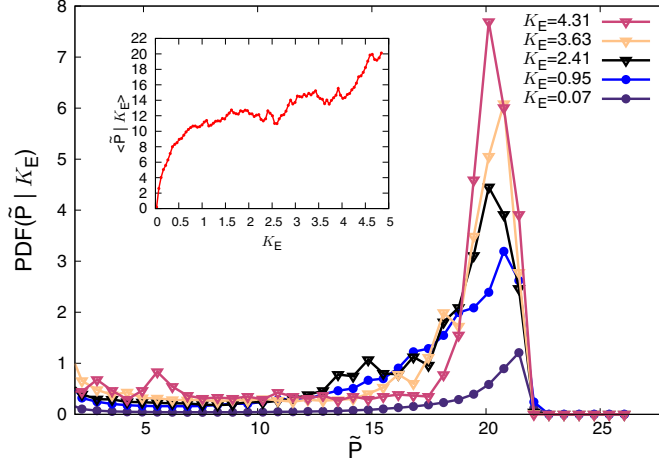
FIG. 8. PDF of $\tilde{P} = P/P_{eq}$ conditioned on the turbulent kinetic energy $\mathcal{K}_E$ at Re = 20 000. The different curves correspond to the PDF conditioned on increasing values of $\mathcal{K}_E$, as reported in the legend. In the inset the conditioned average of $\tilde{P}$ is shown as a function of $\mathcal{K}_E$.

intensity plays a primary role in determining the plankton distribution in space, and, indeed, in the present configuration it promotes biological productivity.

E. Impact of the grid resolution

We now report some results about a comparison between a fully resolved DNS, such as those examined in the previous sections, and two coarse-grained simulations. In this case, the flow and geometrical parameters are the same, but the grid is not sufficiently refined to resolve all the scales in the flow and scalar dynamics. This means that the simulations are under-resolved, and some small-scale effects are lacking. This approach is related to the large-eddy-simulation (LES) one [57], where the unresolved scales are called subgrid scales, and their effect should be reconstructed via some model. Our coarse-grained simulations represent the simplest case in which no subgrid model is taken into account and is referred to in the literature as implicit LES (ILES) [58]. Such a comparison is important since DNS cannot be used to simulate realistic configurations where only a coarse-grained approach is computationally feasible.

We consider the most turbulent case at Re = 20 000. The numerical setup is identical in all cases, except for the maximum level of grid refinement: while for the DNS this is $N = 2^{14}$ and the smallest resolved scale is $\Delta x \sim 1.5 \, \ell_B$, for the coarse-grained simulations we have $N = 2^{12}$ and $\Delta x \sim 6 \, \ell_B$ in the first case, and $N = 2^{10}$ and $\Delta x \sim 25 \, \ell_B$ in the second one. Figures 9(a) and 9(b) show instantaneous phytoplankton density fields at time $t = 200$, for the $N = 2^{12}$ case and the $N = 2^{10}$ one, respectively. While in the left panel the phytoplankton distribution resembles the one observed in the well-resolved DNS (Fig. 1), in the right panel filaments appear thicker and less convoluted; moreover, vortices are not deflected but travel along a straight path, as they would do at lower Re. Concerning the global value of population density [inset of Fig. 9(c)], we can remark that while the case at $N = 2^{12}$ still captures the correct behavior over time, displaying large fluctuations around an average value $\overline{\langle P \rangle}$ which is only slightly lower than that from the fully resolved simulation, when the refinement level is reduced to $N = 2^{10}$, $\overline{\langle P \rangle}$ further decreases and the oscillations around it essentially disappear.

This picture is confirmed by Fig. 9(c), which shows the spectra of phytoplankton fluctuations in the three cases: the spectra at $N = 2^{14}$ and $N = 2^{12}$ are quite similar, except for the decade of the smallest spatial scales, which cannot be captured by the under-resolved simulation; at $N = 2^{10}$,
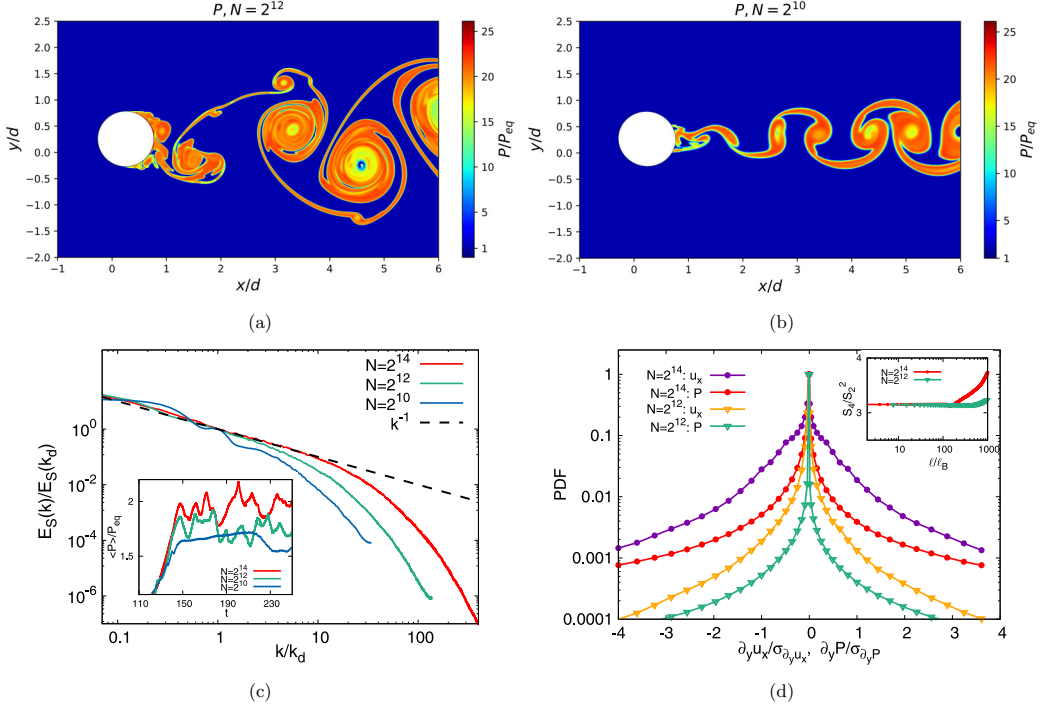
FIG. 9. Panels (a) and (b) show the phytoplankton density field P, at time $t = 200$ and Re $= 20\,000$, for the maximum grid-refinement levels $N = 2^{12}$ and $N = 2^{10}$, respectively. (c) Spectra of phytoplankton fluctuations $E_S(k)$, normalized by $E_S(k_d)$, with k_d the wave number associated with the obstacle diameter d, for Re $= 20\,000$ and $N = 2^{10}, 2^{12}, 2^{14}$. In the inset, the temporal behavior of the spatially averaged phytoplankton density is shown for the same values of Re and N. (d) PDFs of the gradients, in the transversal direction, of longitudinal velocity and phytoplankton density for the simulations with $N = 2^{14}$ (DNS) and with $N = 2^{12}$ (coarse-grained DNS) at Re $= 20\,000$. All PDFs are computed from centered fluctuations, rescaled by the corresponding standard deviation. The inset reports the flatness S_4/S_2^2 of the phytoplankton density field versus the separation ℓ/ℓ_B (with ℓ_B the Batchelor scale) in the transversal direction, for $N = 2^{12}, 2^{14}$.

instead, the spectrum differs from those at higher resolution also at large scales, confirming the inadequacy of this simulation to account for the dynamics at such high Re number. In Fig. 9(d) we show the PDFs of the transversal gradients of the phytoplankton density, representative of the reactive scalar small-scale features, and of longitudinal velocity, for the $N = 2^{14}$ and $N = 2^{12}$ cases. A first remark is that for both the well-resolved DNS and the under-resolved one the P gradients' PDF follows that of the fluid velocity, though with lower tails. More interestingly, it is also apparent that in the coarse-grained case the statistics of large-deviation events are less important, for both $\partial_y P$ and $\partial_y u_x$, so that the PDFs of the latter two fields are narrower and with faster decreasing tails, with respect to the DNS case. To further probe possible effects of the spatial resolution on higher-order statistics, we also computed the flatness of the phytoplankton density field, defined as S_4/S_2^2, where S_2 and S_4 respectively are the second- and fourth-order transversal structure functions of $P(\mathbf{x}, t)$. The behavior of S_4/S_2^2 as a function of the spatial increment ℓ (here in the y direction, and normalized by the Batchelor scale ℓ_B) is presented in the inset of Fig. 9(d). Clearly, for the coarse-grained DNS with $N = 2^{12}$, the smallest separations that are possible to sample are larger than for the well-resolved DNS ($N = 2^{14}$). Beyond this, the results indicate that for $\ell/\ell_B \leqslant 100$, the flatness is close to 3 (the expectation for a Gaussian distribution), but for larger ℓ it starts to deviate from this value, and in the $N = 2^{14}$ case this feature is more evident.

Our analysis suggests that, although a fully resolved simulation allows to grasp all the statistical details of the dynamics, the smallest scales do not seem to have a significant impact on the overall dynamics. Consequently a coarse-grained approach, as in the case with $N = 2^{12}$, appears viable if one is interested in large-scale dynamics (here it is also important to note that with such resolution all the flow scales are resolved, but this is not the case for the scalars, because Sc $\neq$ 1). Instead, a very under-resolved approach ($N = 2^{10}$), in terms of both flow and scalar scales, is misleading and incapable of capturing the correct large- and small-scale dynamics.

F. Effect of the obstacle shape

In this last section, we examine the effect of the obstacle shape. The motivation here comes from the observation that real islands clearly do not have a perfectly circular shape and their boundaries are not necessarily smooth. Indeed, rocky shorelines are known to be well described by fractal curves [59,60]. Therefore, from a general perspective, it is interesting to study the impact on the dynamics of a rough surface delimiting our idealized island. To this aim, we repeated the simulation at Re = 2000 by replacing the circular obstacle with a geometrically irregular shape characterized by a rough boundary, expressed in terms of a truncated Steinhaus series [61]:

$$\rho(\theta) = \rho_0 + A \sum_{k=1}^{\mathcal{N}} (-1 - p)^{1/2} k^{p/2} \cos{(k\theta + \phi_k)}, \tag{7}$$

with $\theta \in [0, 2\pi]$, $\rho_0 = l_0$ (the average radius), $\mathcal{N} = 1000$, $p = -2$, and ϕ_k independent random variables uniformly distributed in $[0, 2\pi]$. The function in Eq. (7) has a power spectral density for all nonzero wave numbers k that decays as $\sim k^p$, where $p = -2\xi - 1$, and is fractal in the limit $\mathcal{N} \to \infty$, with fractal dimension $D_f = 2 - \xi$. In the present case, to have an effect on the turbulent dynamics, the value of A should be chosen such that the corrugations described by $\rho(\theta)$ cross the boundary layer around the obstacle. As the width of the latter can be estimated as $\delta_{BL} \approx \sqrt{\nu l_0 / u_0} \approx 0.04$ (in nondimensional units) at Re = 2000, we chose a value of $A = 0.15$.

As shown in Fig. 10(a), the distribution of plankton near the obstacle for the rough case appears quite different with respect to the smooth one [Fig. 10(c)]: the plankton is entrained in the contour's coves, and its concentration is irregular and variable in time (see the Supplemental Material [52]). Despite these major differences, the downstream patchiness distribution [Fig. 10(b)] as well as the statistical properties are left unchanged. We observe, for example, that the spatially averaged value of population density is very weakly affected by the roughness of the obstacle, with relative variations within the statistical error [inset of Fig. 10(d)] for the cases here explored. This supports the fact that the global excitation of the system is independent of the specific characteristics of boundary layers. Also from the spectra of phytoplankton fluctuations, no appreciable differences could be detected. As shown in Fig. 10(d), the spectra of P fluctuations for the two cases are practically identical over a broad range of scales. The same is true for the velocity field, which displays unchanged spectral scaling far from the obstacle even if the kinetic boundary layer is affected strongly by the roughness. These results indicate that the obstacle roughness does not have a significant impact both on the global and local statistical properties of the advected planktonic species. This appears to be rather independent on the value of characteristic roughness A. Indeed, we verified the robustness of the results also at Re = 400 for $A = 0.15$ and the much rougher case $A = 0.6$. Such a finding, along with the weak dependence on the Reynolds number documented in the previous sections, points to the fact that even at higher values of Re the roughness of the obstacle should not give rise to major modifications of the population dynamics.

V. CONCLUSIONS

We have investigated predator-prey plankton dynamics in turbulent flows occurring in the wake of an obstacle, which is an idealized configuration intended to mimic an island in the ocean. Our purpose was to understand if and how active small flow scales may affect it.
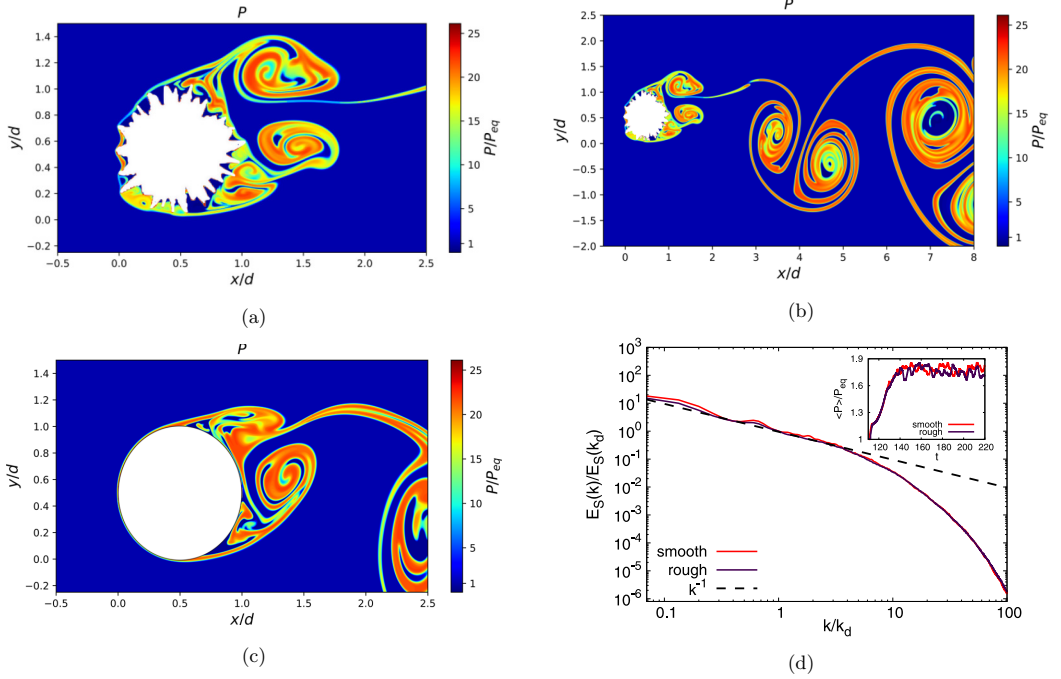
FIG. 10. Visualization of the phytoplankton density field P in the vicinity of the obstacle at time $t = 175$ for: (a) an irregular obstacle with characteristic roughness $A = 0.15$, (c) a smooth cylindrical obstacle, in the same flow conditions. (b) Visualization of phytoplankton density field in the wake generated behind the rough obstacle. (d) Spectra of phytoplankton fluctuations $E_S(k)$ for the smooth obstacle and the rough one, normalized by $E_S(k_d)$, with k_d the wave number associated with the obstacle diameter d. The spectra are computed along the y-direction and averaged over $1.5d \leqslant x \leqslant 10d$ and time. The inset shows the temporal behavior of the spatially averaged phytoplankton density for the two obstacle shapes. In all the panels the Reynolds number is Re = 2000.

Aiming to focus on the role played by the flow field, we chose to limit the complexity of the biological dynamics. In this spirit we adopted the PZ model, perhaps the simplest multi-species system allowing to reproduce the main features of algal blooms [36]. Clearly, this choice poses some limitations on the applicability of our findings to natural environments. Specifically, oligotrophic habitats, where nutrients represent a limiting factor of phytoplankton growth, cannot be described by the present approach. However, since nutrients are not included, and the system is excitable, whenever the flow conditions are capable to trigger a bloom, these model dynamics will sustain it. Furthermore, to evaluate the possible effect of the Reynolds number, we have performed three simulations up to Re = 20 000.

The comparison with previous studies in open flows obtained from kinematic models [5,13,19,28,34,35,42,49] has been instructive, and one of our main results has been to indicate that the key mechanism underlying the blooming is the presence in the flow of at least a region where the biological species remain trapped for very long time. If this feature is encountered, basically the same bloom is triggered irrespective of the precise features of the flow and of the Reynolds number. In fact, as in the case of PZ dynamics in a perturbed-jet kinematic flow [19], in our dynamical turbulent wake, advection needs to be slow enough with respect to the phytoplankton growth, for this to occur. Interestingly, we have been able to detect also a second transition, to de-excitation, for very slow advection, which could not be observed in that study but was found in another kinematic flow [35]. Indeed, in our system an optimal value of order

1 exists for the ratio between flow and biological timescales, which promotes maximum primary production.

We have further found that the presence of a chaotic saddle, whose role had been put in evidence in previous kinematic studies, is not necessarily crucial for blooming, whereas for transport and mixing the details of the fluid dynamics are important. Indeed, we have verified that the plankton bloom occurs even in the laminar regime, and this result allows us to estimate in a simple way the average biomass of the system, which in this case is concentrated in two straight filaments departing from the obstacle, approximately in the streamwise direction, at symmetric positions with respect to the centerline in the cross-stream direction. According to the model developed in [62] for a single reactive tracer in a purely elongational flow, the width ℓ_f of a plankton filament is independent of the biological growth rate and solely determined by the physical parameters of the flow, $\ell_f \sim \sqrt{D/s}$, where D is the effective diffusivity and s the strain rate. In our case, the latter can be dimensionally estimated as $s \sim u_0/\delta_{BL}$, where $\delta_{BL} \sim \sqrt{\nu l_0/u_0}$ is the boundary-layer thickness, which gives $\ell_f \sim (D^2\nu l_0/u_0^3)^{1/4}$. In this way, provided that a patch of population density equal to P_a enters the domain, which is initially at P_{eq}, it is reasonable to expect that the minimum total phytoplankton biomass is given by $P_{\text{tot}} \sim 2P_a\ell_f L_f + P_{eq}L^2$ where L_f is the length of each filament and L the linear domain size. From this, using our parameter values, the average population density, normalized by its equilibrium value, is predicted to be $\overline{\langle P \rangle}/P_{eq} \sim 1.15$, not far from the numerical value of 1.75 that we find at Re = 10. The discrepancy is grasped by considering the reactive nature of phytoplankton, which on average grows in a blooming situation, while being stretched by the flow, before the zooplankton can effectively graze on it.

We have then studied the phenomenology of the small scales at high Re. While the large-scale dynamics, and with it the main characteristics of the bloom, remain basically unchanged, similarly to what reported in previous studies [33,42], a smooth-filamental transition takes place, depending on the relative importance of the strain-rate intensity and the biological growth rate. This point was studied by varying the turbulent intensity in our simulations, instead of the biological parameters as in the case of kinematic flows, which seems to us more interesting in relation to realistic situations. We found that the transition, manifesting as the appearance of fractal features in transects of the P field, occurs at large Reynolds numbers (Re > 2000), when more small scales are present in the velocity field. This suggests that small-scale fluid motions locally affect the fine-scale spatial distribution of the planktonic species, if the flow is turbulent enough. We have also addressed the problem of plankton patchiness by analyzing the spectral properties of P and Z fields, as well as the correlation between the spatial structures of the latter and those of the flow field. Our finding is a neat k^{-1} scaling, over more than two decades, for the variance spectra of the population density fields. This provides a clear indication that reactive scalars are not different from passive (nonreactive) ones with regard to the statistical properties, and lends support to the arguments developed in the framework of simplified theories for interacting species in 2D turbulent flows [25]. This represents a further important result of the present work.

As for the correlation between flow structures and population patchiness, the results previously reported, from both idealized [19,27,28] and realistic models [17,29], or from observations [16–18], are varied, due to the relevance of different mechanisms and the variation of their relative weight in different regions. The results from our simulations provide clear evidence that, in the present setup, phytoplankton mainly concentrates in filamentary structures, winding in the periphery of vortices. At the same time, the biological interactions control the relative abundance of zooplankton and phytoplankton, locally. We hope that such an outcome can contribute to shedding light on the complex organization of plankton with respect to the characteristics of the carrying velocity field, beyond the peculiarities of the flow and biological dynamics here considered. Indeed, some similarities with the present phenomenology have been observed, under some circumstances, also using more realistic biological models [5,27,28].

We have furthermore verified that all these results are *quantitatively* independent of the roughness of the obstacle. For this purpose, we considered idealized islands with different fractal contours [61], as representative of rocky coastlines [60]. This result indicates that the detailed spatial structure of

boundary conditions has, to good extent, a minor role and corroborates the findings highlighting that the mechanism controlling blooms is mainly related to the presence of flow regions trapping the planktonic species.

The last main result of this work concerns the possibility to use a coarse-grained approach instead of resolving all the dynamical scales as here, which is impossible in a realistic situation. We have analyzed simulations with progressively coarser spatial resolution, and our results point out two possibilities with respect to the level of information sought: (1) the dynamics are not very sensitive to small scales, implying that accurate statistical properties at large and intermediate scales can be obtained with a coarser approach, provided such considered scales are resolved; (2) if the focus is only on very large-scale features, for instance, to answer the question *Is there a bloom or not?*, a large-scale approach seems feasible, with the caveat that the statistical properties cannot be well reproduced.

ACKNOWLEDGMENTS

APPENDIX A: NUMERICAL METHOD

Basilisk is an open source code written using an extension to the C programming language, called Basilisk C, for the resolution of partial differential equations (see Ref. [48]). Space is discretized using a Cartesian tree-based grid, which is adaptively varied according to the Re and Sc numbers for well resolving all the scales. Two primary criteria are used to decide where to refine the mesh. They are based on a wavelet decomposition of the velocity, scalar, and volume fraction fields [63]. The velocity and scalar criterion is mostly sensitive to the second derivative of the fields and guarantees refinement in developing boundary layers and wakes. The volume fraction criterion is sensitive to the curvature of the interface and guarantees the accurate description of the shape of the obstacle. Both criteria are usually combined with a maximum allowed level of refinement. Boundaries of general shape are reconstructed using an integral (i.e., finite volume) formulation, which takes into account the volume and area fractions of intersection of the embedded boundary with the mesh [64]. The numerical scheme implemented in Basilisk is described, e.g., in [65]. The Navier-Stokes equations are integrated by a projection method [66]. Standard second-order numerical schemes for the spatial gradients are used [65,67,68]. In particular, the velocity advection term $\partial_j(u_j u_i)^{n+1/2}$ is estimated by means of the Bell-Colella-Glaz second- or third-order unsplit upwind scheme [67]. In this way, the problem is reduced to the solution of a Helmholtz-Poisson problem for each primitive variable and a Poisson problem for the pressure correction terms. Both the Helmholtz-Poisson and Poisson problems are solved using an efficient multilevel solver [67,69]. The time advancing is made through a fractional-step method using a staggered discretization in time of the velocity and the scalar fields [65]: one supposes the velocity field to be known at time n and the scalar fields (pressure, density, plankton) to be known at time $n - 1/2$, and one computes velocity at time $n + 1$ and scalars at time $n + 1/2$.

In all the simulations, we adopted the following boundary conditions for the flow:

$$[u_n]_{\text{left}} = u_0, \tag{A1a}$$

$$[u_t]_{\text{left}} = 0, \tag{A1b}$$

$$[\partial_n u_n]_{\text{right}} = 0, \tag{A1c}$$

$$[\partial_n u_t]_{\text{right}} = 0, \tag{A1d}$$

$$[u_n]_{\text{top}} = [u_n]_{\text{bottom}} = 0, \tag{A1e}$$

$$[\partial_n u_t]_{\text{top}} = [\partial_n u_t]_{\text{bottom}} = 0, \tag{A1f}$$

$$[u_n]_{\text{obstacle}} = [u_t]_{\text{obstacle}} = 0; \tag{A1g}$$
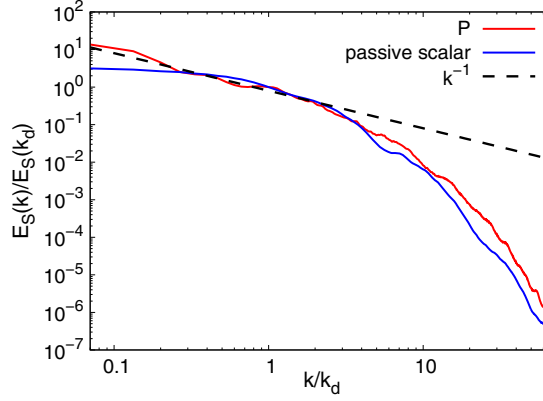
FIG. 11. Spatial spectra of phytoplankton density and nonreactive passive scalar fluctuations $E_S(k)$, normalized by $E_S(k_d)$, with k_d the wave number associated with the obstacle diameter. The spectra are computed along the y-direction and averaged over $1.5d \leqslant x \leqslant 10d$ and time.

i.e., an inflow or outflow condition is imposed on the left or right side of the domain, while free-slip conditions hold at the boundaries in the y-direction and a no-slip condition on the obstacle. The subscripts n and t stand for the normal and tangential component, respectively, relative to the boundary walls. In order to avoid issues with inconsistent boundary conditions, we introduced a damping layer near the in- and out-flow boundaries.

Concerning the two scalars, they are kept at the equilibrium values (P_{eq}, Z_{eq}) at all sides of the domain, while on the obstacle no-flux conditions are imposed:

$$[\partial_n P]_{\text{obstacle}} = 0, \tag{A2a}$$

$$[\partial_n Z]_{\text{obstacle}} = 0. \tag{A2b}$$

APPENDIX B: COMPARISON WITH A PASSIVE SCALAR

In order to better understand the effect of the growth dynamics, and of the biological interactions, on plankton spectra, we performed a simulation at Re = 400 (with a smooth circular obstacle) considering a passive, nonreactive scalar, obeying the same equations as those for the planktonic species, except for the reaction term, which is now removed. The choice of this particular value of Re was motivated by the low computational cost. The boundary conditions are the same as those adopted for the phytoplankton, except for the condition on the obstacle, where we impose a Dirichlet boundary condition by choosing a constant value higher than in the surroundings (we also verified that the specific numerical value has no impact on the dynamics). Our focus is here on possible differences induced by the reactive evolution in comparison to the passive one. We expected that these differences, if they exist, could be visible at large scales where the biological activity is predominant with respect to the turbulent environmental effects [20,25]. In Fig. 11 the spectra of the phytoplankton density, as well as of the nonreactive tracer, fluctuations at Re = 400 are shown. In both cases, the spectrum is compatible with a $\sim k^{-1}$ scaling in the enstrophy inertial range, before a steeper fall-off, typical of a viscous range, at larger wave numbers. Generally, the plankton spectrum appears to follow the -1 slope at scales larger than the injection scale, where the passive scalar spectrum is flatter.

[1] K. Mann and J. Lazier, *Dynamics of Marine Ecosystems: Biological-Physical Interactions in the Oceans* (Wiley, New York, 2005).

[2] R. G. Williams and M. J. Follows, *Ocean Dynamics and the Carbon Cycle: Principles and Mechanisms* (Cambridge University Press, Cambridge, 2011).

[3] K. G. Sellner, G. J. Doucette, and G. J. Kirkpatrick, Harmful algal blooms: Causes, impacts and detection, J. Ind. Microbiol. Biotechnol. **30**, 383 (2003).

[4] M. Kahru and B. G. Mitchell, Ocean color reveals increased blooms in various parts of the world, Eos **89**, 170 (2008).

[5] K. Guseva and U. Feudel, Numerical modelling of the effect of intermittent upwelling events on plankton blooms, J. R. Soc. Interface **17**, 20190889 (2020).

[6] K. L. Denman and A. E. Gargett, Biological-physical interactions in the upper ocean: The role of vertical and small scale transport processes, Annu. Rev. Fluid Mech. **27**, 225 (1995).

[7] J. Huisman, M. Arrayás, U. Ebert, and B. Sommeijer, How do sinking phytoplankton species manage to persist?, Am. Nat. **159**, 245 (2002).

[8] C. Lindemann, A. Visser, and P. Mariani, Dynamics of phytoplankton blooms in turbulent vortex cells, J. R. Soc. Interface **14**, 20170453 (2017).

[9] E. Abraham, The generation of plankton patchiness by turbulent stirring, Nature (London) **391**, 577 (1998).

[10] A. P. Martin, K. J. Richards, A. Bracco, and A. Provenzale, Patchy productivity in the open ocean, Glob. Geochem. Cycles **16**, 9-1 (2002).

[11] A. P. Martin, Phytoplankton patchiness: The role of lateral stirring and mixing, Prog. Oceanog. **57**, 125 (2003).

[12] R. Reigada, R. M. Hillary, M. A. Bees, J. M. Sancho, and F. Sagués, Plankton blooms induced by turbulent flows, Proc. R. Soc. London B **270**, 875 (2002).

[13] C. López, Z. Neufeld, E. Hernández-García, and P. H. Haynes, Chaotic advection of reacting substances: Plankton dynamics on a meandering jet, Phys. Chem. Earth B **26**, 313 (2001).

[14] L. Goodman and A. R. Robinson, On the theory of advective effects on biological dynamics in the sea. III. The role of turbulence in biological-physical interactions, Proc. R. Soc. London A **464**, 555 (2008).

[15] M. Lévy, The modulation of biological production by oceanic mesoscale turbulence, Lect. Notes Phys. **744**, 219 (2008).

[16] D. J. J. McGillicuddy, Mechanisms of physical-biological-biogeochemical interaction at the oceanic mesoscale, Annu. Rev. Mar. Sci. **8**, 125 (2016).

[17] M. Lévy, P. J. S. Franks, and K. S. Smith, The role of submesoscale currents in structuring marine ecosystems, Nat. Commun. **9**, 4758 (2018).

[18] Z. Zhang, B. Qiu, P. Klein, and S. Travis, The influence of geostrophic strain on oceanic ageostrophic motion and surface chlorophyll, Nat. Commun. **10**, 2838 (2019).

[19] E. Hernández-García and C. López, Sustained plankton blooms under open chaotic flows, Ecol. Complex. **1**, 253 (2004).

[20] K. L. Denman and T. Platt, The variance spectrum of phytoplankton in a turbulent ocean, J. Mar. Res. **34**, 593 (1976).

[21] R. C. Smith, X. Zhang, and J. Michaelsen, Variability of pigment biomass in the California Current System as determined by satellite imagery. 1. Spatial variability, J. Geophys. Res. **93**, 10863 (1988).

[22] A. P. Martin and M. A. Srokosz, Plankton distribution spectra: Inter-size class variability and the relative slopes for phytoplankton and zooplankton, Geophys. Res. Lett. **29**, 66-1 (2002).

[23] M. Lévy and P. Klein, Does the low frequency variability of mesoscale dynamics explain a part of the phytoplankton and zooplankton spectral variability?, Proc. R. Soc. London A **460**, 1673 (2004).

[24] P. Franks, Plankton patchiness, turbulent transport and spatial spectra, Mar. Ecol. Prog. Ser. **294**, 295 (2005).

[25] T. M. Powell and A. Okubo, Turbulence, diffusion and patchiness in the sea, Philos. Trans. R. Soc. London B **343**, 11 (1994).

[26] C. Pasquero, A. Bracco, and A. Provenzale, Coherent vortices, Lagrangian particles and the marine ecosystem, in *Shallow Flows*, edited by W. Uijttewaal and G. Jirka (Balkema Publishers, Leiden, 2004), p. 399.

[27] M. Sandulescu, C. López, E. Hernández-García, and U. Feudel, Plankton blooms in vortices: The role of biological and hydrodynamic timescales, Nonlin. Proc. Geophys. **14**, 443 (2007).

[28] M. Sandulescu, C. López, E. Hernández-García, and U. Feudel, Biological activity in the wake of an island close to a coastal upwelling, Ecol. Complex. **5**, 228 (2008).

[29] I. Hernández-Carrasco, V. Rossi, E. Hernández-García, V. Garçon, and C. López, The reduction of plankton biomass induced by mesoscale stirring: A modeling study in the Benguela upwelling, Deep-Sea Res. I **83**, 65 (2014).

[30] V. Rossi, C. López, J. Sudre, E. Hernández-García, and V. Garçon, Comparative study of mixing and biological activity of the Benguela and Canary upwelling systems, Geophys. Res. Lett. **35**, L11602 (2008).

[31] V. Rossi, C. López, E. Hernández-García, J. Sudre, V. Garçon, and Y. Morel, Surface mixing and biological activity in the four eastern boundary upwelling systems, Nonlin. Proc. Geophys. **16**, 557 (2009).

[32] Z. Toroczkai, G. Károlyi, Á. Péntek, T. Tél, and C. Grebogi, Advection of Active Particles in Open Chaotic Flows, Phys. Rev. Lett. **80**, 500 (1998).

[33] Z. Neufeld, C. López, E. Hernández-García, and T. Tél, Multifractal structure of chaotically advected chemical fields, Phys. Rev. E **61**, 3857 (2000).

[34] Z. Neufeld, Excitable Media in a Chaotic Flow, Phys. Rev. Lett. **87**, 108301 (2001).

[35] Z. Neufeld, C. López, E. Hernández-García, and O. Piro, Excitable media in open and closed chaotic flow, Phys. Rev. E **66**, 066208 (2002).

[36] J. E. Truscott and J. Brindley, Ocean plankton populations as excitable media, Bull. Math. Biol. **56**, 981 (1994).

[37] J. E. Truscott and J. Brindley, Equilibria, stability and excitability in a general class of plankton population models, Philos. Trans. R. Soc. London A **347**, 703 (1994).

[38] M. Sandulescu, E. Hernández-García, C. López, and U. Feudel, Kinematic studies of transport across an island wake, with application to the Canary islands, Tellus A **58**, 605 (2006).

[39] J. D. Murray, *Mathematical Biology* (Springer-Verlag, New York, 2002).

[40] P. Grindrod, *Patterns and Waves: Theory and Applications of Reaction-Diffusion Equations* (Oxford University Press, Oxford, 1991).

[41] C. S. Holling, The components of predation as revealed by a study of small-mammal predation of the European pine sawfly, Can. Entomol. **91**, 293 (1959).

[42] E. Hernández-García, C. López, and Z. Neufeld, Small-scale structure of nonlinearly interacting species advected by chaotic flows, Chaos **12**, 470 (2002).

[43] Z. Neufeld, P. H. Haynes, V. Garçon, and J. Sudre, Ocean fertilization experiments may initiate a large scale phytoplankton bloom, Geophys. Res. Lett. **29**, 1534 (2002).

[44] M. Polin, I. Tuval, K. Drescher, J. Gollub, and R. Goldstein, Chlamydomonas swims with two gears in a eukaryotic version of run-and-tumble locomotion, Science **325**, 487 (2009).

[45] M. Garcia, S. Berti, P. Peyla, and S. Rafaï, Random walk of a swimmer in a low-Reynolds-number medium, Phys. Rev. E **83**, 035301(R) (2011).

[46] M. Brun-Cosme-Bruny, E. Bertin, B. Coasne, P. Peyla, and S. Rafaï, Effective diffusivity of micro-swimmers in a crowded environment, J. Chem. Phys. **150**, 104901 (2019).

[47] G. Boffetta and R. Ecke, Two-dimensional turbulence, Annu. Rev. Fluid Mech. **44**, 427 (2012).

[48] http://basilisk.fr.

[49] D. Bastine and U. Feudel, Inhomogeneous dominance patterns of competing phytoplankton groups in the wake of an island, Nonlin. Proc. Geophys. **17**, 715 (2010).

[50] M. D. Van Dyke, *An Album of Fluid Motion* (Parabolic, Stanford, CA, 1982).

[51] M. M. Zdravkovich, *Flow Around Circular Cylinders, Vol. 1: Fundamentals* (Oxford University Press, Oxford, 1997).

[52] See Supplemental Material at http://link.aps.org/supplemental/10.1103/PhysRevFluids.6.103802 for dynamic visualizations of phytoplankton density fields.

[53] R. H. Kraichnan, Inertial ranges in two-dimensional turbulence, Phys. Fluids **10**, 1417 (1967).

[54] G. K. Batchelor, Small-scale variation of convected quantities like temperature in turbulent fluid Part 1. General discussion and the case of small conductivity, J. Fluid Mech. **5**, 113 (1959).

[55] D. Ruelle, Microscopic fluctuations and turbulence, Phys. Lett. A **72**, 81 (1979).

[56] I. Hernández-Carrasco, C. López, E. Hernández-García, and A. Turiel, Seasonal and regional characterization of horizontal stirring in the global ocean, J. Geophys. Res. **117**, C10007 (2012).

[57] S. B. Pope, *Turbulent Flows* (Cambridge University Press, Cambridge, 2001).

[58] F. F. Grinstein, L. G. Margolin, and W. J. Rider, *Implicit Large Eddy Simulation* (Cambridge University Press, Cambridge, 2007).

[59] B. Mandelbrot, How long is the coast of Britain? Statistical self-similarity and fractional dimension, Science **156**, 636 (1967).

[60] G. Boffetta, A. Celani, D. Dezzani, and A. Seminara, How winding is the coast of Britain? Conformal invariance of rocky shorelines, Geophys. Res. Lett. **35**, L03615 (2008).

[61] S. Toppaladoddi, A. J. Wells, C. R. Doering, and J. S. Wettlaufer, Thermal convection over fractal surfaces, J. Fluid Mech. **907**, A12 (2021).

[62] A. P. Martin, On filament width in oceanic plankton distributions, J. Plank. Res. **22**, 597 (2000).

[63] J. A. van Hooft, S. Popinet, C. C. van Heerwarrden, S. J. A. van der Linden, S. R. de Roode, and B. J. H. van de Wiel, Towards adaptive grids for atmospheric boundary-layer simulations, Bound.-Layer Meteor. **167**, 421 (2018).

[64] H. Johansen and P. Colella, A Cartesian grid embedded boundary method for Poisson's equation on irregular domains, J. Comput. Phys. **147**, 60 (1998).

[65] S. Popinet, An accurate adaptive solver for surface-tension-driven interfacial flows, J. Comput. Phys. **228**, 5838 (2009).

[66] A. J. Chorin, On the convergence of discrete approximations to the Navier-Stokes equations, Math. Comp. **23**, 341 (1969).

[67] S. Popinet, Gerris: A tree-based adaptive solver for the incompressible Euler equations in complex geometries, J. Comput. Phys. **190**, 572 (2003).

[68] P. Y. Lagrée, L. Staron, and S. Popinet, The granular column collapse as a continuum: Validity of a two-dimensional Navier-Stokes model with a $\mu(I)$-rheology, J. Fluid Mech. **686**, 378 (2011).

[69] S. Popinet, A quadtree-adaptive multigrid solver for the Serre–Green–Naghdi equations, J. Comput. Phys. **302**, 336 (2015).